Article

^{40}Ar/^{39}Ar dating reveals over 30 million years of plume-ridge interaction formed the Rio Grande Rise

Check for updates

Peter C. Davidson [1,2] ✉, Anthony A. P. Koppers [1], Cornelia Class [3], William W. Sager[4] & Daniel Heaton[1]

The Rio Grande Rise (RGR) oceanic plateau exhibits distinctly broad morphology compared to the linear, age-progressive Walvis Ridge (WR), despite both originating from the Tristan-Gough (T-G) plume. New ^{40}Ar/^{39}Ar ages (84–41 Ma) from RGR demonstrate prolonged coeval formation with WR at the Mid-Atlantic Ridge (MAR) during a ridge-centered plume configuration. These plume-ridge interactions coincided with a temporary microplate eventually incorporated into the South American Plate, explaining RGR's broader spatial distribution. Backtracking reveals that absolute plate motion and southward plume drift shut off excess magma supply when the T-G plume moved south of large lateral MAR offsets, ending volcanism on the South American plate around 52 Ma—later than previously estimated. Although RGR's erupted volume matches large igneous provinces, magmatic production rates were moderate, resembling modern-day Iceland rather than high-flux terrestrial large igneous provinces. This supports a ridge-centered plume origin over a high-flux magma pulse, demonstrating how plume-ridge configuration and microplate tectonics controlled the evolutionary divergence of these related South Atlantic volcanic features.

The Rio Grande Rise (RGR) is an oceanic plateau located in the southwest Atlantic Ocean on the South American plate (Fig. 1a). Its large spatial extent and volume[1] has led some to consider it a large igneous province (LIP)[1–3], implying a rapid formation based on the common definition of a LIP[4]. However, its formation history remains poorly constrained due to little available geochronology, leaving its geodynamic origin uncertain.

RGR is considered the conjugate of the older Walvis Ridge (WR), with both thought to have formed together at the Mid-Atlantic Ridge (MAR) axis sometime in the Cretaceous[2,5–7]. Both RGR and WR are thought to be expressions of the same Tristan-Gough (T-G) hotspot, attributed to a mantle plume currently active below Tristan da Cunha and Gough islands on the African Plate[8]. Recent studies on samples from the southeast RGR support this connection by showing geochemical similarities to WR and the T-G hotspot[3,9].

Despite their supposed shared origin, RGR and WR differ greatly in their morphology: RGR forms a broad feature, whereas WR is continuous and comparatively narrow, and extends westward as younger seamounts of the WR Guyot Province on the African plate, which have no conjugate on the South American plate. These differences imply different expressions of the T-G hotspot on either side of the MAR, the underlying geodynamic processes of which remain unclear.

RGR has a complex structure that includes several massifs, tectonic basins, and rift zones (Fig. 1b). Deep Sea Drilling Project (DSDP) Hole 516F cored into the basement of the W(est)-RGR producing ^{40}Ar/^{39}Ar ages from 82.0 ± 0.5 to 86.0 ± 4.0 Ma[7,10,11]. Eocene age volcaniclastic sediments were also recovered from DSDP Hole 516F[11]. This late stage Eocene volcanism is also found in 46 Ma alkaline lavas dredged from sites along the Cruzeiro do Sul Rift[7,12] which is a large rift valley of unknown origin trending NW-SE that dissects both the W- and SE-RGR (Fig. 1). These initial sparse age data suggest that RGR could have had a prolonged eruptive history with multiple periods of construction, similar to other oceanic plateaus[13–15] and oceanic mid-plate superstructures[16].

The WR is also complex and includes several sub-regions, each with their own unique characteristics. The oldest portion, nearest the African continent, is the E-W trending Frio Ridge which formed around 115 Ma[7] (Fig. 1a). This transitions into the N-S trending Valdivia Bank (VB) which is thought to be the conjugate of W-RGR, forming together at the MAR between ~90 and 80 Ma[2,6,7]. Around 29 °S WR changes from a

[1]College of Earth, Ocean, and Atmospheric Sciences, Oregon State University, Corvallis, OR, USA. [2]GEOMAR Helmholtz Centre for Ocean Research Kiel, Kiel, Germany. [3]Lamont-Doherty Earth Observatory of Columbia University, Palisades, NY, USA. [4]Department of Earth and Atmospheric Sciences, University of Houston, Houston, TX, USA. ✉e-mail: p.davidson.geo@gmail.com
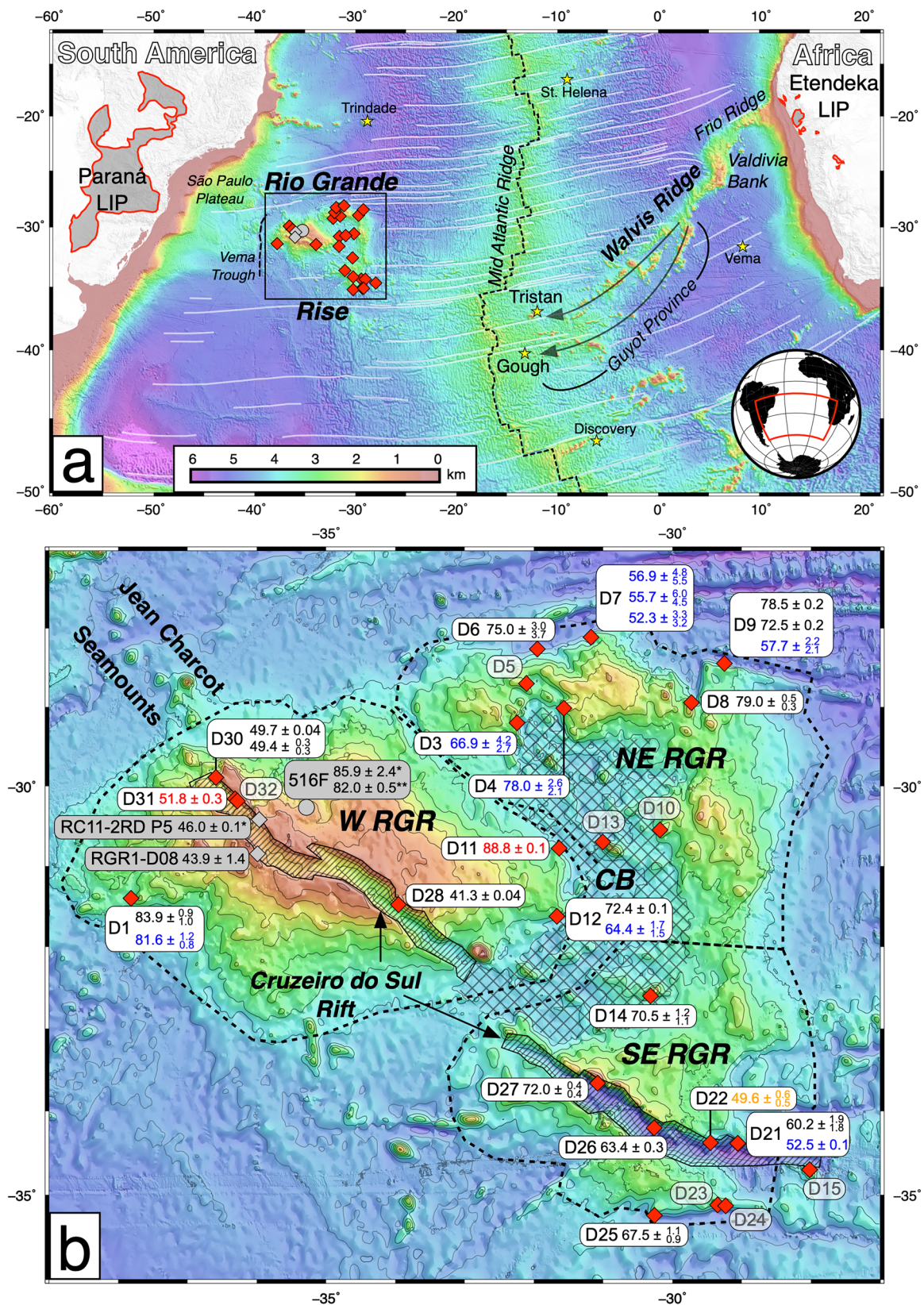
relatively continuous bathymetric high into a ~ 400 km wide region of seamounts—called the Guyot Province—that trend southwest towards the modern MAR. The WR Guyot Province contains two isotopically distinct and age progressive seamount trails, the Tristan Track and Gough Track[7,17–21]. Although the Gough Track can be traced back to the

earliest stages of the WR, the Tristan Track does not emerge until the WR splits into the Guyot Province at about 70 Ma[18,19], which is when the T-G hotspot is thought to have become intraplate under the African plate only. Recent isotopic data show that the Jean Charcot Seamounts and parts of RGR have Tristan affinities that extend back perhaps to ~100 Ma

Fig. 1 | Bathymetric maps of the South Atlantic and Rio Grande rise.
a Bathymetric map of the South Atlantic Ocean. The continental surface expressions of the Paraná and Etendeka LIPs are outlined in red, filled gray. The Mid-Atlantic Ridge (MAR) is denoted by the center black dashed line and the Vema Trough (thought to be an extinct spreading center[2]) is marked by a dashed line west of RGR. The two arrows in WR indicate the two geochemical subtracks of the WR Guyot Province[18,19], with Tristan to the north and Gough to the south. Labeled yellow stars indicate the approximate locations of currently active hotspots. **b** Close-up bathymetric map of RGR with labeled dredge and drill (DSDP Hole 516 F) locations (diamonds and circle, respectively) and ages (in Ma). Red diamonds are dredge locations from cruise NBP1808 (this study) while three gray locations are from other campaigns that also produced ages[7,10,12]. Eruption ages are shown in black font, eruption age estimations in grey, minimum eruption ages in blue, maximum eruption ages in red. All uncertainties are 2σ standard errors, stacked uncertainties are 97.5% (top) and 2.5% (bottom) confidence intervals using weighted kernel density estimations (WKDE). Dashed outlines show our distinction of sub-provinces: West (W-RGR), Northeast (NE-RGR), and Southeast RGR (SE-RGR) as individual sub-regions that are roughly separated by the Centaurus Basin (CB, hatched pattern). The Cruzeiro do Sul Rift (lined pattern) incises both W- and SE-RGR. Maps were created in GMT[70] and use GEBCO bathymetry[71].

on the South American Plate, suggesting that Tristan and Gough are both long-lived plume components[9].

Several aspects of the RGR-WR system make it an important case study for hotspots and large igneous provinces (LIPs). The T-G plume system is one of only a few hotspots with a continuous record of volcanism from the present back to the proposed inception of volcanism in the form of a LIP[22]. It is also notable in that the plume appears to have produced multiple episodes of high-volume volcanism: the Paraná-Etendeka Flood Basalts (135–132 Ma[23,24]), and RGR and VB (~ 90–80 Ma[7,10,11,21]). Because the size of RGR is similar to the Paraná and other LIPs, some have speculated that RGR may also result from high-flux, LIP volcanism. Importantly however, the LIP nature of RGR has so far been unclear due to a lack of geochronological evidence. In addition, the T-G plume system seems to have been located at or near the MAR axis for a long period with influence on this spreading ridge and the South Atlantic asthenosphere[9,25–28]. Both the RGR and WR also have experienced late-stage Eocene off-axis volcanism that cannot be attributed to the T-G plume system.

Understanding the combined geochemical and geochronological history of RGR therefore is critical in advancing our knowledge on the geodynamics of the overall T-G plume system, its influence on the geochemical makeup of South Atlantic asthenosphere, and its relationship with the opening of the South Atlantic basin. While WR has received considerable attention with numerous sampling campaigns, RGR was sparsely sampled until recently, and first-order questions about its emplacement history remain unanswered[3,9,29,30]. This paper presents a broad geochronologic history of RGR, examines its relationship to WR, and evaluates the role of the T-G plume in its creation.

Results

Thirty-nine analyses from 36 individual samples in 19 dredge locations were dated by incremental step heating $^{40}Ar/^{39}Ar$ analysis[31]. A summary of the results can be found in Table 1 with more detailed results in Supplementary Notes 1 and 2. Many samples show non-ideal degassing behavior due to the difficulties of dating old, very low-K, submarine LIP basalts[32] and some degree of alteration (Supplementary Note 3). The increased resolution from ARGUS-VI mass spectrometers equipped with 10^{13} Ω resistors measuring ^{39}Ar, ^{38}Ar and ^{37}Ar, an electron multiplier measuring ^{36}Ar, and only the large ^{40}Ar signal being measured by a 10^{12} Ω resistor, resulted in highly precise measurements for each step, despite low K content for most samples. This high precision combined with some amount of (likely) alteration resulted in many samples showing scatter among consecutive steps, and therefore high calculated MSWD values. High MSWD values themselves do not rule out these samples from being considered reliable age plateaus[33], but the highly precise individual steps do result in calculated weighted mean age uncertainties that are unrealistically small given the amount of scatter among individual step ages (Fig. 2b). Another way of quantifying their uncertainty must be used.

We use a tiered system to decide which age and associated uncertainty is best for a given experiment. The first (and default) tier is the standard weighted mean plateau age and 2σ standard error (e.g., Fig 2a). If a sample's plateau age MSWD is higher than the MSWD 2σ confidence interval, the next tier is the inverse isochron age and 2σ standard error. If a sample's inverse isochron MSWD is also higher than its MSWD 2σ confidence interval, then the final tier is a weighted kernel density estimation (WKDE)

and 2.5% and 97.5% confidence intervals (a 95% confidence envelope) are used for the uncertainty. Here the MSWD 2σ confidence interval (or $MSWD_{max}$) is defined as the maximum MSWD expected given the number of data, given by the expression:

$$MSWD_{max} = 1 + 2 \times (2/n - 2)^{1/2} \quad (1)$$

where n corresponds to the number of steps in the age plateau or inverse isochron[34,35]. An MSWD > $MSWD_{max}$ means that the amount of scatter among the steps is greater than what can be expected given the analytical uncertainties of individual steps with 95% confidence[34]. Increasing numbers of steps in an age plateau or isochron decreases this $MSWD_{max}$ towards a value of 1. Increasing the analytical resolution of individual steps tends to cause MSWD values to increase. In modern high-resolution mass spectrometry we are typically increasing the number of steps in experiments while decreasing analytical uncertainties, which taken together are resulting in MSWD and $MSWD_{max}$ values diverging in opposite directions. This is in part why many of our measured sample MSWDs fall outside their $MSWD_{max}$ limit.

WKDEs are generated assuming a Gaussian age distribution for each individual step and weighing each step by the amount of $^{39}Ar_{(K)}$ released (i.e., the step size, calculated as a percentage of the total amount released in the entire experiment). This results in age density distributions that allow us to calculate the 2.5% and 97.5% confidence intervals (encompassing a 95% confidence envelope) as an estimation of the uncertainty for each age, and the median is used for the age estimation itself. Our WKDEs are generally less precise but appear to better capture the actual uncertainty in analyses with moderate to considerable scatter (e.g., Fig 2b). Importantly, all the WKDE median ages are within the 2σ standard error of the calculated standard weighted mean plateau age (supplementary Table 1), but the only thing that changes to any considerable degree is the associated uncertainty of the age. WKDE uncertainties are on average about 3.5X larger than the standard weighted mean age uncertainty. Despite this increase, the 2σ uncertainties of individual WKDEs are still about ± 3% (average) and as little as 0.1% (in a few samples). This is more than sufficient to address geodynamic questions about RGR's formation.

Analyses from 36 samples sourced from 16 dredge locations yielded 10 eruption ages, eight eruption age estimations, six minimum eruption age estimations, one maximum eruption age estimation, and 10 samples did not yield a reliable age. An additional sample (NBP1808-D11-01) yields an age plateau from a glass analysis, but this likely contains excess ^{40}Ar, and is therefore an overestimation of the age, and is not further considered in the discussion (Supplementary Note 4). NBP1808-D31-06 is considered a maximum age because it displays a slight stepwise decrease in age from low to high-T steps. Minimum ages are often interpreted as minimums due to evidence of $^{40}Ar^*$ loss in low-T steps and slight saddle shapes (see Supplementary Note 7 for age spectra), evidence of sericitization[36]. Altogether, our ages for RGR range from 83.6 to 41.3 Ma.

Several dredges recovered samples that span a large variation in age (e.g., dredges NBP1808-D7, -D9, -D12, and -D21). These dredged locations with high escarpments along the periphery of the sub-plateaus, or in the case of NBP1808-D21 from the deeply incised Cruzeiro do Sul Rift. These all dredged between 850 and 1650 m of vertical stratigraphy with deep starting depths between 4050 and 5250 m. Samples from these locations contain a

Table 1 | Summary of ages

Sample Name	Phase	Steps used/ Total steps	Preferred Model	Interpretation	Preferred Age [Ma]	±2 SE	-2.5% CI	+97.5% CI	Δ Age [Ma]
West Rio Grande Rise									
NBP1808-D01-01	Plag	12/26	WKDE Median	Eruption age estimation	83.60		−1.36	+1.13	16.1
NBP1808-D01-11	Plag	16/26	WKDE Median	Min. eruption age estimation	81.87		−1.40	+2.21	17.8
NBP1808-D11-01	Glass	12/27	Plateau Age	Excess 40Ar*	88.81	±0.21			−9.5
NBP1808-D12-33	Plag	10/22	Inverse Isochron Age	Eruption age	72.35	±0.22			6.2
NBP1808-D12-42	Plag	10/21	WKDE Median	Eruption age estimation	64.42		−1.69	+2.02	14.2
NBP1808-D28-06	Bt	13/42	Plateau Age	Eruption age	41.27	±0.05			44.2
NBP1808-D30-07	Bt	35/59	Inverse Isochron Age	Eruption age	49.69	±0.04			55.1
NBP1808-D30-18	Plag	10/21	Plateau Age	Eruption age	49.47	±0.05			55.3
NBP1808-D31-06	Cpx	12/19	WKDE Median	Max. eruption age estimation	51.88		−2.84	+3.38	54.0
Northeast Rio Grande Rise									
NBP1808-D03-03	Plag	6/21	Plateau Age	Min. eruption age	66.50	±0.41			18.9
NBP1808-D04-39	Plag	20/27	WKDE Median	Min. eruption age estimation	78.06		−2.79	+3.20	6.1
NBP1808-D06-18	Plag	18/29	WKDE Median	Eruption age estimation	75.00		−4.39	+3.50	4.3
NBP1808-D07-01	Plag	10/26	WKDE Median	Eruption age estimation	52.26		−3.71	+3.78	24.0
NBP1808-D07-15	Plag	10/21	WKDE Median	Eruption age estimation	56.91		−6.36	+5.57	19.3
NBP1808-D07-27	Plag	13/25	WKDE Median	Min. eruption age estimation	50.57		−3.79	+5.88	25.6
NBP1808-D07-95	Plag	12/21	WKDE Median	Min. eruption age estimation	55.67		−5.39	+6.92	20.6
NBP1808-D08-14	Plag	13/29	Plateau Age	Eruption age	79.74	±0.11			−2.0
NBP1808-D09-14	Plag	11/26	WKDE Median	Eruption age estimation	57.72		−2.38	+2.53	18.5
NBP1808-D09-33	Plag	13/22	Plateau Age	Eruption age	78.47	±0.22			-2.3
NBP1808-D09-60	Plag	9/26	Plateau Age	Eruption age	72.48	±0.21			3.7
Southeast Rio Grande Rise									
NBP1808-D21-06	Plag	12/22	WKDE Median	Min. eruption age estimation	52.02		−2.17	+2.46	11.2
NBP1808-D21-10	Plag	5/18	WKDE Median	Eruption age estimation	60.24		−1.77	+1.89	3.0
NBP1808-D25-01-NL	Glass	8/27	WKDE Median	Eruption age estimation	67.15		−1.45	+1.45	−3.9
NBP1808-D26-01	Plag	12/15	Plateau Age	Eruption age	63.98	±0.51			5.1
NBP1808-D26-27	Plag	14/24	Plateau Age	Eruption age	63.15	±0.35			5.9
NBP1808-D27-12	Plag	10/21	WKDE Median	Min. eruption age estimation	71.82		−1.93	+1.73	0.2

Uncertainties for weighted kernel density estimations (WKDEs) are given as the 2.5% confidence interval (negative value) and the 97.5% confidence interval (positive value), uncertainties for age plateaus are given as the 2 standard error. Mineral phase abbreviations *Plag* plagioclase, *Bt* biotite, *Cpx* clinopyroxene, *Gm* groundmass.

variety of textures and mineralogy (see Supplementary Note 5 for detailed petrography) indicating that they come from different volcanic events. This, along with their variations in age shows that these locations were erupted over a prolonged period, encompassing multiple eruptive events that record a prolonged emplacement history. The longest duration of volcanism was sampled at NBP1808-D9, where volcanism spans over 20 Myr from initial eruptions at 78.5 Ma to as late as 57.8 Ma.

In the geographical age distribution, it is notable that W-RGR ages span the entire age range and include a distinctly younger group of Eocene ages (51.9–41.3 Ma) that all come from dredges along the Cruzeiro do Sul rift (Fig. 1b). However, when excluding these Eocene ages, the W-RGR is the oldest portion of RGR ranging from 83.6 to 64.4 Ma. The NE-RGR and SE-RGR also have wide age ranges, but somewhat younger, ranging from 79.7 to 50.6 Ma and 71.8 to 52.0 Ma, respectively.

Therefore, all three sub-regions have overlapping eruptive histories, indicating that RGR as a whole has an emplacement history that spans >30 Myrs.

Discussion

Prolonged emplacement of Rio Grande Rise with Walvis Ridge

RGR has long been assumed to be a LIP due to its large size and the volume of lava produced[1]. Our new ages demonstrate that RGR was emplaced over a prolonged period in stark contrast to the conventional understanding that LIPs are rapidly emplaced features[4]. As a result of more detailed geochronology studies, prolonged emplacement of oceanic LIPs is increasingly observed. This includes the largest oceanic LIPs: Ontong Java and Kerguelen, which are also the best sampled, and both have emplacement timescales >5 Myrs and Kerguelen perhaps up to 30 Myrs[14,37]. In contrast,
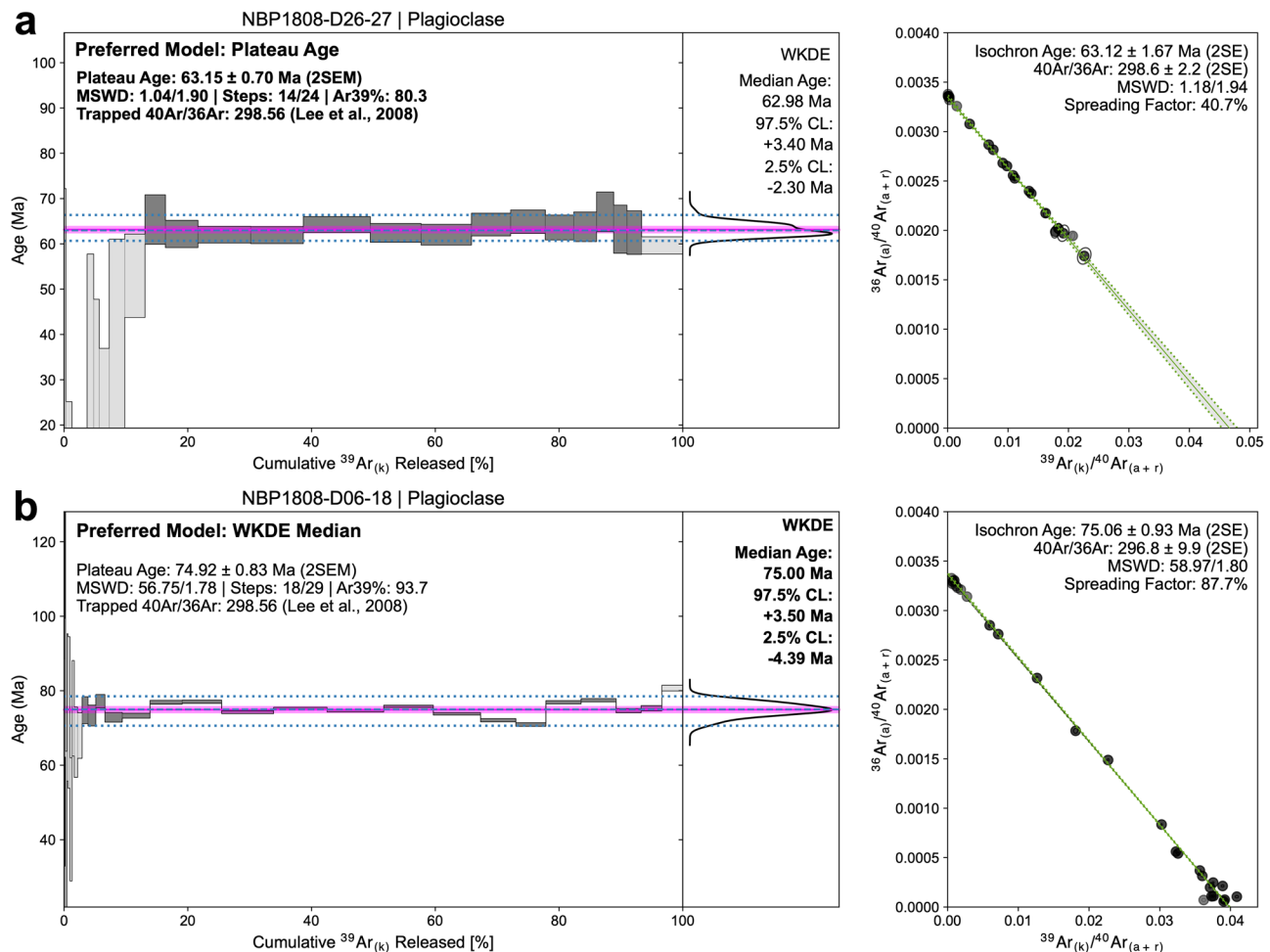
Fig. 2 | Example ^{40}Ar/^{39}Ar age spectra, weighted kernel density estimations (WKDEs), and inverse isochrons. a NBP1808-D26-27 is a sample where the traditional age plateau is preferred and (**b**) NBP1808-D06-18 is a sample where the WKDE is preferred, an example of an experiment that has increased scatter resulting in a high MSWD (> 50, and much higher than the MSWD$_{max}$ = 1.78) and an unrealistically low weighted mean age plateau uncertainty of ± 0.83 Ma (2σ standard error). The WKDE 2.5% and 97.5% confidence intervals (blue dotted lines) do a better job of capturing this sample's uncertainty (+ 3.49, −4.40 Ma), and all the individual steps fall inside this range. The magenta line denotes the ArArCALC weighted mean age and its height the weighted mean plateau age 2σ standard error.

terrestrial LIPs such as the Deccan, Paraná and Siberian Traps were largely emplaced in <1 Myr[38–40].

Despite the many new dates for RGR in this study and the large age database that exists for WR, the earliest stages of emplacement remain unclear. Our ages from NBP1808-D01 (83.6 & 81.9 Ma) are similar to the oldest ages from DSDP Hole 516F in W-RGR and those from the southeast VB in WR[7,21], but these ages are few and come from large volcanic features. In addition, DSDP Hole 516F is located near the center of W-RGR and the penetration is shallow, so it does not capture the earliest phases of volcanism. Given the broad range of ages that exists between DSDP Hole 516F and our other two locations in W-RGR (85.9–64.4 Ma), an earlier phase may exist and could extend the emplacement of W-RGR further back in time. The initial emplacement of W-RGR and VB likely coincided with an eastward ridge jump that left the Vema Trough, an abandoned spreading center, on the South American Plate (Fig. 1a) around the end of the Cretaceous Quiet Period[2,41]. The younger Eocene ages (51.9–41.3 Ma) from three locations in W-RGR must be part of a distinct, late stage eruptive event[7,12] based on the different composition of samples compared to the older locations. Our ages indicate that this Eocene event was more widespread and occurred over a longer period—at least 10 Myrs—than previously known (see further discussion below).

Our spatio-temporal resolution is higher for the emplacement of NE-RGR and SE-RGR (21 ages from 11 locations) compared to W-RGR. W-RGR and VB appear to be conjugate features given their similar ages, but this implies that NE-RGR does not have a conjugate feature on the African Plate. Current plate reconstructions place the MAR within NE-RGR and increasingly further away from VB between 75 and 65 Ma (Fig. 3), which would require an asymmetric accretion of overthickened crust on the South American plate, but normal crust on the African plate, a configuration contradicted by a typical symmetric overthickening of crust for active ridge-centered plumes (e.g., Iceland). This discrepancy could be solved by the presence of a temporary microplate that was later incorporated into the South American plate[2,42], a scenario that is not yet incorporated into available plate reconstruction models of the South Atlantic[41,43]. Four locations in the NE-RGR produced ages between 80 and 75 Ma and, of these, the oldest three samples are located 180-230 km away from each other, indicating they could have erupted on conjugate spreading centers that form the edges of this microplate (Fig. 3). In this scenario, an eastward ridge jump likely incorporated the microplate (and the entire NE-RGR) into the South American plate by Chron C32n.1n (71.4 Ma)[44] and regular spreading resumed afterwards (as shown in Fig. 3 in the 65 Ma panel).

The SE-RGR is the conjugate to the WR segment where it bifurcates into the discontinuous Guyot Province (Fig. 3). This is an important region as it corresponds to the emergence of the Tristan sub-track on the African Plate near the 29°S WR bifurcation point (Fig. 1A). It is suggested that this bifurcation occurred when the T-G plume transitioned from being ridge-centered to intraplate on the African Plate only at ~70 Ma[18,19]. Our ages from
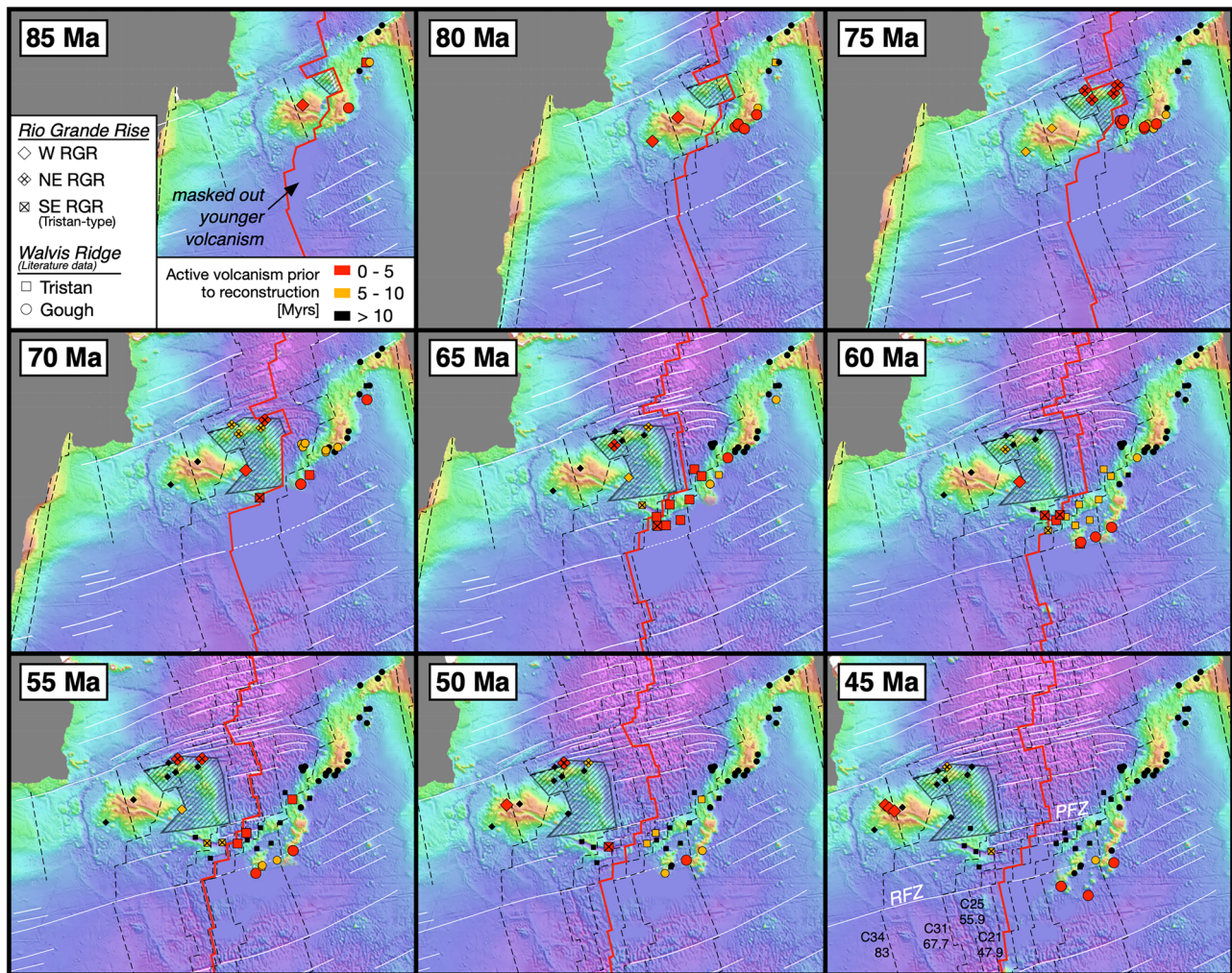
Fig. 3 | Plate tectonic reconstructions of the South Atlantic from 85 to 45 Ma. Reconstructions were made in GPlates[72] using the rotation parameters of Zahirovic et al.[73] and plotted in GMT[70]. Each dated panel shows the locations of dated samples from RGR (this study) and WR[6,7,10,11,20,21]. Symbol color denotes timing of volcanism relative to reconstruction age. Active volcanism (within 5 Myrs of the reconstruction time) is shown by red symbols, recently active (within 5-10 Myrs) by orange symbols, and inactive (> 10 Myrs) by black symbols. The hatched region indicates the approximate area of a proposed microplate[2] now incorporated into the South American plate. The red line is the paleo-MAR, white lines are fracture zones including PFZ Peleg Fracture Zone, RFZ Rachel Fracture Zone, and dashed black lines are isochrons (labeled in the 45 Ma plot with chron numbers and ages in Ma) from Seton et al.[43].

SE-RGR extend as young as 52 Ma and imply that this did not occur for at least another 10 Myrs. After 52 Ma, volcanism occurred only on the African plate (Fig. 3, 45 Ma), producing the WR Guyot Province[7,18–20,26] and volcanism ceased on the South American plate, except for the further afield Eocene volcanism in the W-RGR.

Late-stage Eocene volcanism
Three dredge sites (NBP1808-D28, -D30 and -D31) located along the Cruzeiro do Sul Rift in the W-RGR yielded Eocene ages ranging from 51.9 to 41.3 Ma. Two of these sites are located near DSDP Site 516 and two dredge sites (RC11-2RD and RGR1-D08; Fig. 1B) previously provided evidence of Eocene volcanism[7,12]. Most samples dredged from throughout RGR are plagioclase or olivine-phyric, or aphyric tholeiitic basalts, which are indicative of high degrees of partial melting. Our Eocene samples come from alkalic rock types, some of which include biotite phenocrysts, further indicating the difference between these samples and the older main-phase samples from the W-RGR. This compositional difference indicates that these young ages are not younger alteration ages, but in fact a separate, later and lower-degree (and deeper) melting event. NBP1808-D30 and -D31 are located northwest in the W-RGR and along its crest, providing further evidence of late-stage volcanism in the region near previously dated examples[7,12]. NBP1808-D28 is located southeast in the W-RGR, and extends the known region of this late-stage event to almost the full ~300 km length of the Cruzeiro do Sul Rift in the W-RGR. This shows that Eocene volcanism was more geographically widespread than previously known, possibly over the whole W-RGR and indicating that this likely was a major rejuvenated magmatic event.

The Eocene volcanism in the W-RGR could be related to the nearby Jean-Charcot Seamounts that bisect a portion of the W-RGR and that are geochemically similar[3]. Eocene volcanism is somewhat age-progressive (Fig. 4) and co-parallel with the (scattered) age progression of RGR itself. The direction of the Jean-Charcot Seamounts is also co-parallel to the overall trend of volcanism on the South American plate, which is generally progressing towards the southeast. No ages are currently available from the Jean-Charcot Seamounts, but it is possible that the Eocene volcanism that is capping the older eruptive portion of the W-RGR is a younger extension of the Jean-Charcot Seamount volcanism, creating a co-parallel set of age-progressive volcanism. This is in contrast to the model of Homrighausen et al.[9], who suggested they are older (~ 100–80 Ma) based on their guyot-like structures and predicted crustal subsidence models. They suggested that the Jean-Charcot Seamounts are therefore related to the main eruptive phase of W-RGR. Extending the

age progression of the W-RGR Eocene volcanism to the Jean-Charcot Seamounts would imply that its northwestern-most seamount formed approximately 65 Ma, about 35 Myrs later than the ages proposed by Homrighausen et al.[9] (Fig. 4).
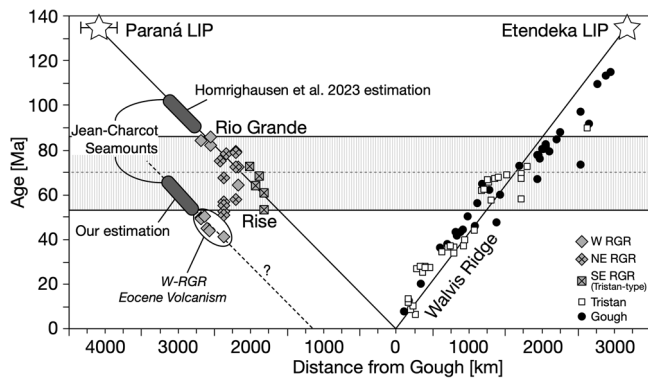

Fig. 4 | Age vs distance from Gough Island. RGR is generally age-progressive. The Jean-Charcot Seamounts could either be age-progressive with respect to the main-phase of RGR (Homrighausen et al.[9] model), or with respect to the late-stage Eocene volcanism at W-RGR (our model). Note that we have shown the Jean-Charcot seamounts schematically with the oval field which spans the distance from the nearest to closest from Gough, while in reality there are over 20 individual seamounts.

On- versus off-axis emplacement

Comparing the eruption age of a sample to the age of the underlying seafloor gives the age of the oceanic lithosphere at the time that the sample was erupted. This Δ age of a sample (Table 1) is calculated by subtracting the sample age from the modeled age of the seafloor, using the age model of Seton et al.[43] for the latter.

The SE-RGR and more than half of the NE-RGR erupted at or very near the MAR axis between ~85 and 60 Ma, while W-RGR erupted more off-axis (Fig. 5). Near-zero Δ age values indicate that excess volcanism was active at the ridge axis while increasing Δ age values indicate progressively greater distance of off-axis emplacement. With a half spreading rate of 25 km Myr^{-1} (roughly the rate at this time in the South Atlantic), a sample with a Δ age = 5 Myr was emplaced 125 km off the ridge axis. Given the volume and flux of lavas erupted to form RGR, which is upwards of 2000–3000 m above the surrounding seafloor and with a total crustal thickness of ~25 km[45], it is likely that individual eruptive vents were not all centered directly at the MAR axis. Flows were also likely able to travel some distance from vents, up to tens or hundreds of kilometers, as has been shown from other submarine eruptions[46,47]. Therefore, samples with Δ age <5 Myr (< 125 km) are considered to have erupted on-axis; and samples with a Δ age = 5–10 Myr near-axis (125–250 km).

Overall, almost all volcanism throughout the RGR occurred between ~85 and 55 Ma (hatched region in Fig. 5a) and was mostly on-axis or near-axis of the MAR. Several locations in the NE-RGR and one in SE-RGR show continued (off-axis) volcanism for >10 Myr, after the oldest initial RGR

Fig. 5 | Δ Age of RGR and WR samples. a Sample age vs Δ age for RGR (gray symbols) and WR (black circles = Gough track, white squares = Tristan track). The shaded blue region is considered on axis. Walvis Ridge ages are from refs. 6,7,10,20,21 and RGR literature ages are from refs. 7,10,12. **b** Bathymetric map showing the locations and Δ age (colors of symbols) of all samples with ages from RGR and Walvis Ridge. Symbols are the same as A), the MAR is the red line down the center and gray lines are fracture zones. Map made in GMT[70].
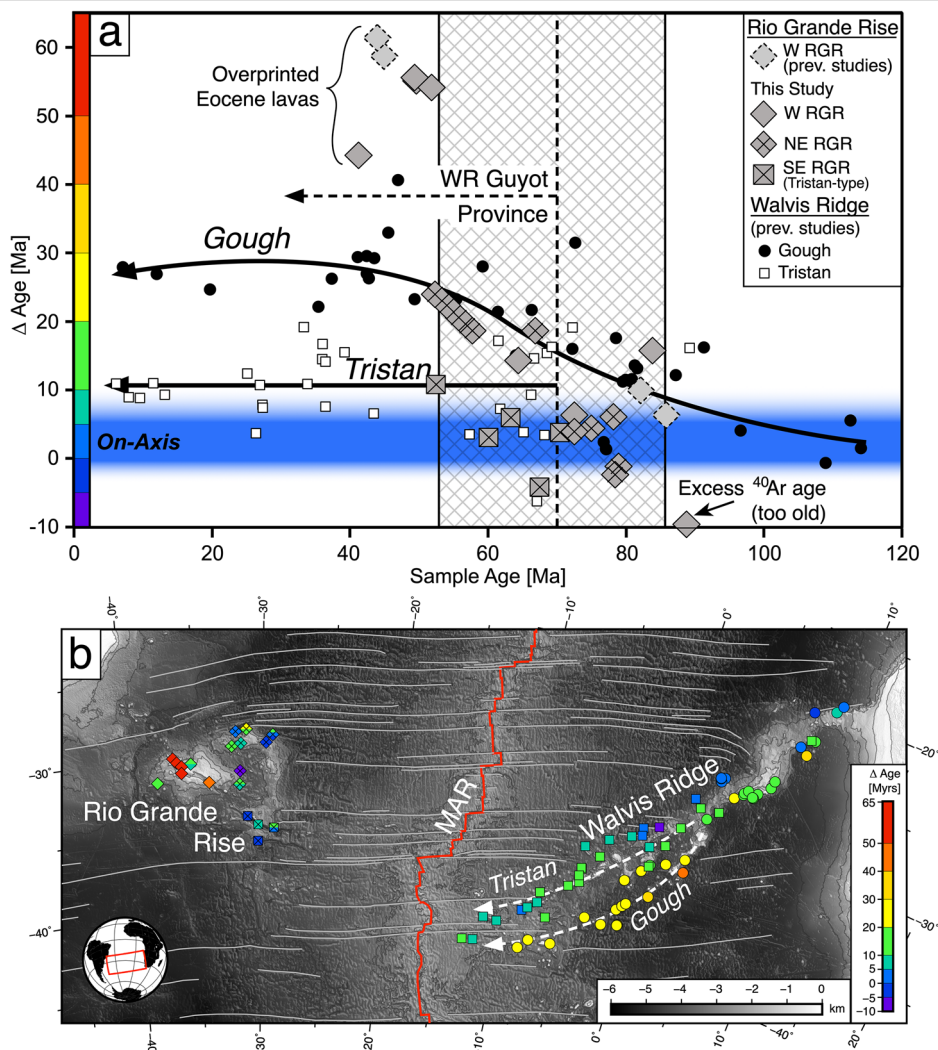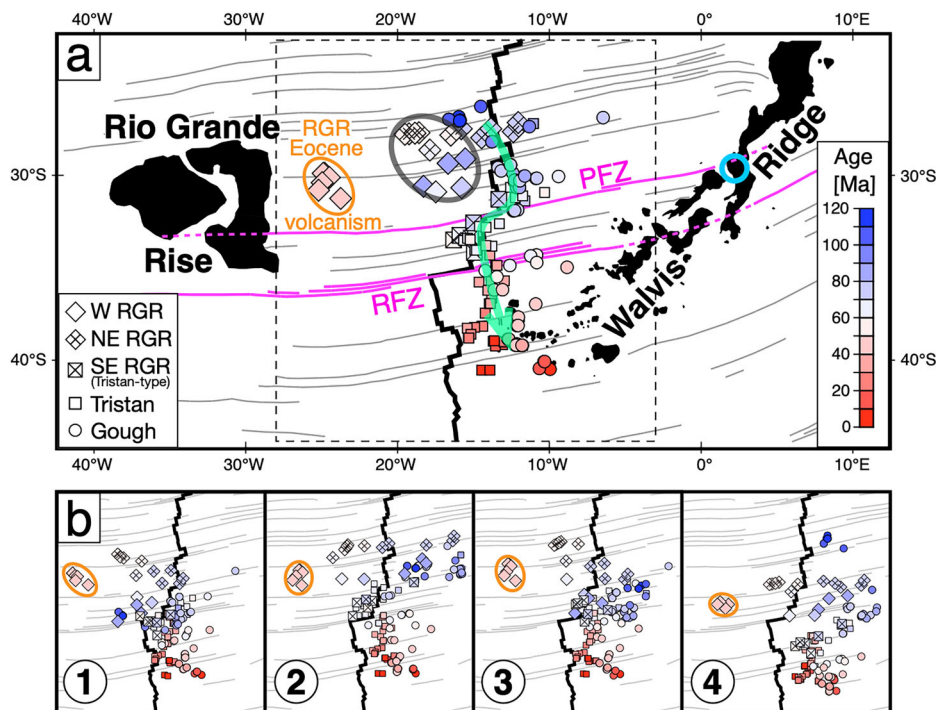
Fig. 6 | Backtracked locations of RGR and WR volcanism. a Rotated to the modern ridge using half-stage rotation parameters of Pérez-Díaz & Eagles[41]. **b** Four different absolute plate motion models, which show the location of T-G plume volcanism relative to the modern ridge, and a general southward motion of the plume through time. Absolute plate motion models used: 1 = mantle reference frame[49], 2 = moving hotspots model[48], 3 = moving hotspots model[50], 4 = global hybrid model[50]. WR ages come from the same references as those in Fig. 3. Colors correspond to the age of each sample. The MAR is the thick black line in the middle of each panel, fracture zones are grey lines with two important fracture zones highlighted in magenta in panel (**a**): PFZ Peleg Fracture Zone, RFZ Rachel Fracture Zone. The dotted portions of these extend into the regions of the RGR and WR where they are overprinted by volcanism. The blue circle in (**a**) shows the bifurcation point of WR, note that this occurs exactly where the PFZ intersects WR. W-RGR late-stage Eocene volcanism is circled in orange. Other off and near-axis volcanism during the formation of W-RGR and late stages of NE-RGR is circled in grey in panel (**a**). The green arrow in (**a**) shows the apparent westward shift in WR volcanism at PFZ and the shift to the African Plate only south of the RFZ. The dotted black box in (**a**) outlines the areas in panel b. Each map was made in GMT[70].

eruptions. The locations with highest Δ age values (dredges NBP1808-D7, -D9, -D12, and -D21) all come from places that dredged large portions (> 800 m) of the volcanic stratigraphy (Supplementary Note 5) and suggest that volcanism continued up to ~450 km off the ridge axis.

Three dredge locations at RGR contain negative Δ age values ranging from −2.0 to −3.9 Myr, indicating that the current age model needs refinement in this region during the Cretaceous[43]. These negative Δ age values from the RGR are coincident with slightly positive Δ age values from the WR (Fig. 5a), which may suggest that the paleo-MAR was slightly more east compared to the current reconstructions. The proposed microplate or ridge jumps[2,42] could also account for such minor errors in the plate reconstructions.

Long-term Tristan-Gough plume interaction with the Mid-Atlantic ridge

Backtracked locations of RGR and WR volcanism using half-stage poles of the South American and African Plates[41] show where those samples were erupted relative to the present-day MAR geometry (Fig. 6a). This shows that T-G volcanism migrated from north to south relative to the ridge by some combination of absolute plate motion and/or plume motion. Some absolute plate motion and plume motion models also indicate southward plume drift (Fig. 6b)[48–50] but these models are subject to considerable uncertainty further back in time, in particular prior to 60–80 Ma. This southward migration of volcanism crosses what we are calling the Peleg and Rachel Fracture Zones (PFZ & RFZ: named after the closest named seamounts in the WR) during the time at which volcanism transitioned from being MAR-centered to intraplate (Fig. 6a). Together, the PFZ and RFZ account for > 450 km of lateral offset of the MAR spreading axis and they mark the southern extent of the microplate activity[42]. Magnetic isochrons show that this lateral offset

of the paleo-MAR was also present, with a similar offset distance, at least as far back as the late Cretaceous[41] (Fig. 3). We postulate that this combined large offset, in conjunction with the southward migration of the T-G plume (relative to the MAR), is responsible for the transition from MAR-centered to intraplate volcanism on the African Plate.

With the exception of some late-stage volcanism that occurred off the ridge axis (e.g. RGR Eocene volcanism, circled in orange in Fig. 6), volcanism north of the PFZ lasted from ~120 Ma until ~70 Ma and was largely ridge centered. However, this Cretaceous volcanism also is characterized by a spatial variability around the MAR that is likely the result of the elevated magma fluxes forming W-RGR and NE-RGR and VB, which are the most voluminous portions of the RGR and WR, respectively. Some samples in the NE-RGR (included in the grey circle in Fig. 6) appear to have formed more off-axis, but we offer that they also could have formed as part of the microplate, which had two or more overlapping spreading segments separated by an unknown, but likely substantial (> 100 km), distance. The less voluminous SE-RGR was formed between the PFZ and RFZ, at the time of bifurcation of WR into the Guyot Province (Figs. 3 & 6). This began at ~70 Ma and continued until ~55 Ma, during the time period when the T-G plume was transitioning from being ridge-centered to off-axis[10]. This largely fits with the model put forward by Homrighausen et al.[9] with distinct Tristan and Gough 'plumelets' straddling the MAR prior to ~70 Ma, with the northwestern Tristan plumelet finally crossing the MAR by 60 Ma.

An eastward migration of the MAR around the PFZ and RFZ occurred sometime between Chron 34 and 25 (83.6–57.1 Ma), resulting in asymmetric crustal accretion (Supplementary Fig. 4). This is the time and place of SE-RGR emplacement and, as discussed, during the time when the plume was transitioning from ridge-centered to intraplate. There is also an apparent westward (from north to south) shift of WR volcanism

immediately south of the PFZ (light green arrow in Fig. 6a) concurrent with the westward lateral offset of the MAR at PFZ and the bifurcation of the WR. This could indicate that the T-G plume and MAR were trying to remain coupled during this period between ~70 and 60 Ma. This resulted in shifting the ridge eastward and the plume westward, pulling each other towards a common center. South of the RFZ, and from 60 Ma to the present day, volcanism became entirely intraplate, restricted to the African Plate only, and decoupled from the ridge.

Changes in the Tristan-Gough Plume Production Rate through Time

Changes in the T-G plume magmatic production rate have been estimated in several previous studies[51–53]. These assumed a perfectly age-progressive hotspot track in which active magmatism occurs along a transect perpendicular to a line fitted through the hotspot track. These methods allow for a granular estimation of flux through time, but they neglect the fact that magmatism of this scale is distributed over a wide spatial area at any given time. Furthermore, only one estimation included both the VB, RGR, and volcanism >80 Ma[51], and these studies all assumed that the entirety of RGR is >70 Ma, which we have shown is incorrect. Our geochronological record of RGR allows us to more accurately include it into estimations of the long-term T-G plume production rate.

It has been debated whether or not part of RGR is continental in origin[5,29,30,45]. Old continental crust was recovered in dredges[29], but were described as being subrounded and covered in Mn-crust, suggesting they may be dropstones instead of in-situ crustal material. Geophysical evidence is inconclusive regarding a possible continental crustal component of RGR[45]. Geochemical evidence, however, indicates no evidence of continental influence (via assimilation) of the definitively in-situ basalts recovered from RGR during expedition MSM-82[3]. Therefore, while we acknowledge that new evidence could find evidence that part of RGR is continental in origin, we assume that all of RGR is basaltic in nature.

We use residual bathymetry to find the volume of erupted lava throughout RGR and WR, using the volume above the base level, characterized by a break in slope at the 800 m contour (Supplementary Fig. 5). In this analysis we use the residual bathymetry (Fig. 7a) from CEED (https://www.earthdynamics.org/page5.html) which uses lithospheric thermal subsidence from Crosby & McKenzie[54] and the isostatic correction method from Sykes[55] with sediment thicknesses subtracted from the GEBCO (2014) grid[56]. We then use the excess magmatic volume grid from Huang & Li[52] (Fig. 7b) to also calculate the total excess magma produced which includes the crustal root. Both calculations were done using GMT grdvolume and subdivided into a number of areas: RGR into W, NE, and SE; and WR into VB and its Guyot Province into 10 Myr increments based on literature ages of WR volcanism[6,7,10,20,21] (Fig. 7). Our method averages the production rate over these respective areas, which has the advantage of not assuming a perfectly age-progressive nature of the T-G hotspot, but the disadvantage in that it misses shorter period pulses or variations in the production rate.

The entirety of RGR has an erupted volume of $\sim 6.7 \times 10^5$ km^3, similar to the Deccan Traps[57], and nearly 9.1×10^5 km^3 when including VB in WR (but not the younger Guyot Province or Frio Ridge; Table 2). This is still less than half the erupted volume of the Siberian Traps and the Paraná-Etendeka, each with erupted volumes $>20 \times 10^5$ km^3[39,58] and is an order of magnitude less than the Ontong Java Plateau with an erupted volume $>80 \times 10^5$ km^3[59]. The total erupted volume of the T-G hotspot from the emplacement of W-RGR/VB to the present day, including the WR Guyot Province, is $\sim 15 \times 10^5$ km^3. Maximum eruption rates were about 0.03 km^3 yr^{-1} during the emplacement of W-RGR/VB, less than modern-day Hawai'i[60].

Total magmatic volumes are on average ~5.5X greater than erupted volumes in the combined RGR and WR. Maximum total magmatic production rate estimations (total excess volume) indicate that the entirety of RGR and VB (RGR + VB) were ~0.26 km^3 yr^{-1} (Table 2). W-RGR is the most voluminous portion of the three sub-regions (about 3/5 of the total volume, and nearly half when adjusted for surface area) and has a total

production rate of ~0.15 km^3 yr^{-1}. VB and NE-RGR have slightly lower rates of ~0.10 to 0.13 km^3 yr^{-1}. The SE-RGR formed at a much lower rate of about 0.03 km^3 yr^{-1}, further suggesting that the T-G hotspot was waning in strength, even before the plume had become entirely intraplate[53]. This could explain why the T-G plume did not have the strength to (re)capture the MAR after it moved across the PFZ and RFZ as it reportedly did successfully at the end of the Cretaceous Quiet Period[2,41]. After the plume became entirely intraplate in the WR Guyot Province, production rates averaged ~0.03 km^3 yr^{-1} from 50 Ma to the present, similar to other estimates[53].

Assuming an average full spreading rate of 5 cm yr^{-1} in the South Atlantic, the magmatic production rate at the ridge is 3.5×10^{-4} km^3 yr^{-1} per ridge km (km^3 km^{-1} yr^{-1}). To compare this with the total T-G plume production rates, we must normalize the latter rates to the diameter of the plume affecting the MAR. The plume's diameter is estimated to be 400 km based on the spatial extent of volcanism in the Guyot Province, which in turn is close to the N-S length of RGR and VB. Production rates normalized to this 400 km ridge length are highest during the emplacement of W-RGR and VB at 7×10^{-4} km^3 km^{-1} yr^{-1}, and when we add this to MAR production, this essentially triples the overall magmatic output in this region. This combined rate decreases in the SE-RGR and the 60-70 Ma portion of the Guyot Province (the conjugate to the SE-RGR) to $<2.5 \times 10^{-4}$ km^3 km^{-1} yr^{-1}. After the plume moved off the ridge axis after 50 Ma, the overall production rate was reduced even further to $<1 \times 10^{-4}$ km^3 km^{-1} yr^{-1}.

A present analog to RGR is Iceland, which is a modern example of a mantle plume centered at (or near) a spreading ridge axis. Iceland is an extensively studied volcanic system with complex plume-ridge interactions that have influenced the expression of the plume as well as the northern MAR over the past >20 Myr[61]. Total magmatic production rates in Iceland are estimated to be ~0.25 to 0.30 km^3 yr^{-1}[62,63] and thus about the same as the combined W-RGR/VB, supporting their similar geodynamic origins. Other modern examples of ridge-centered plumes include the Galapagos and Azores, which have similar magmatic production rates between ~0.14 and 0.30 km^3 yr^{-1}[62,64]. The correspondence in magma production rates between the RGR and Iceland, Galapagos, and Azores supports a mantle plume stem centered on a ridge axis having formed RGR, and not a secondary high-flux pulse of the T-G plume.

RGR/VB eruption rates are much lower than terrestrial LIP equivalents, such as the Deccan and Siberian Traps, and the Paraná-Etendeka, which all three had eruption rates >1 km^3 yr^{-1} and pulsed peak rates much higher still[23,38,39]. It is possible that RGR and VB had peak production rates higher than the long-term averages we are calculating, but limited sampling prevents us from resolving these peak rates. However, to approach rates similar to the Deccan and Siberian Traps, the entirety of RGR/VB would have had to have been emplaced in <1 Ma. Given the broad geochronological coverage now available, this appears highly unlikely, implying that eruption rates for RGR/VB emplacement were one to two orders of magnitude less than terrestrial LIPs. This establishes that, despite the similarities in size and volume between RGR and terrestrial LIPs, the emplacement dynamics of RGR were quite different. According to the definition of Bryan & Ernst[4] LIPs are characterized by igneous pulse(s) of short 1–5 Myr duration, during which >75% of the total igneous volume has been emplaced. RGR therefore does not qualify as a LIP based on the Bryan and Ernst definition. Other oceanic plateaus (e.g., Ontong Java, Kerguelen, Shatsky Rise) also do not meet this rapid formation criteria[14,37,65], and yet are still commonly ascribed as LIPs. The vast differences in magmatic production rate among LIPs, including oceanic plateaus, likely results from important differences among their geodynamic origins (i.e., a plume head vs a plume stem interacting with a spreading center) and this also likely plays a role in the differences of their environmental impacts[66].

Methods
^{40}Ar/^{39}Ar dating
Thirty-two locations were dredged from RGR and the surrounding area (see Supplementary Note 2 for a dredging summary). Thirty-five samples from 19 dredge locations were chosen for ^{40}Ar/^{39}Ar analysis. Samples were
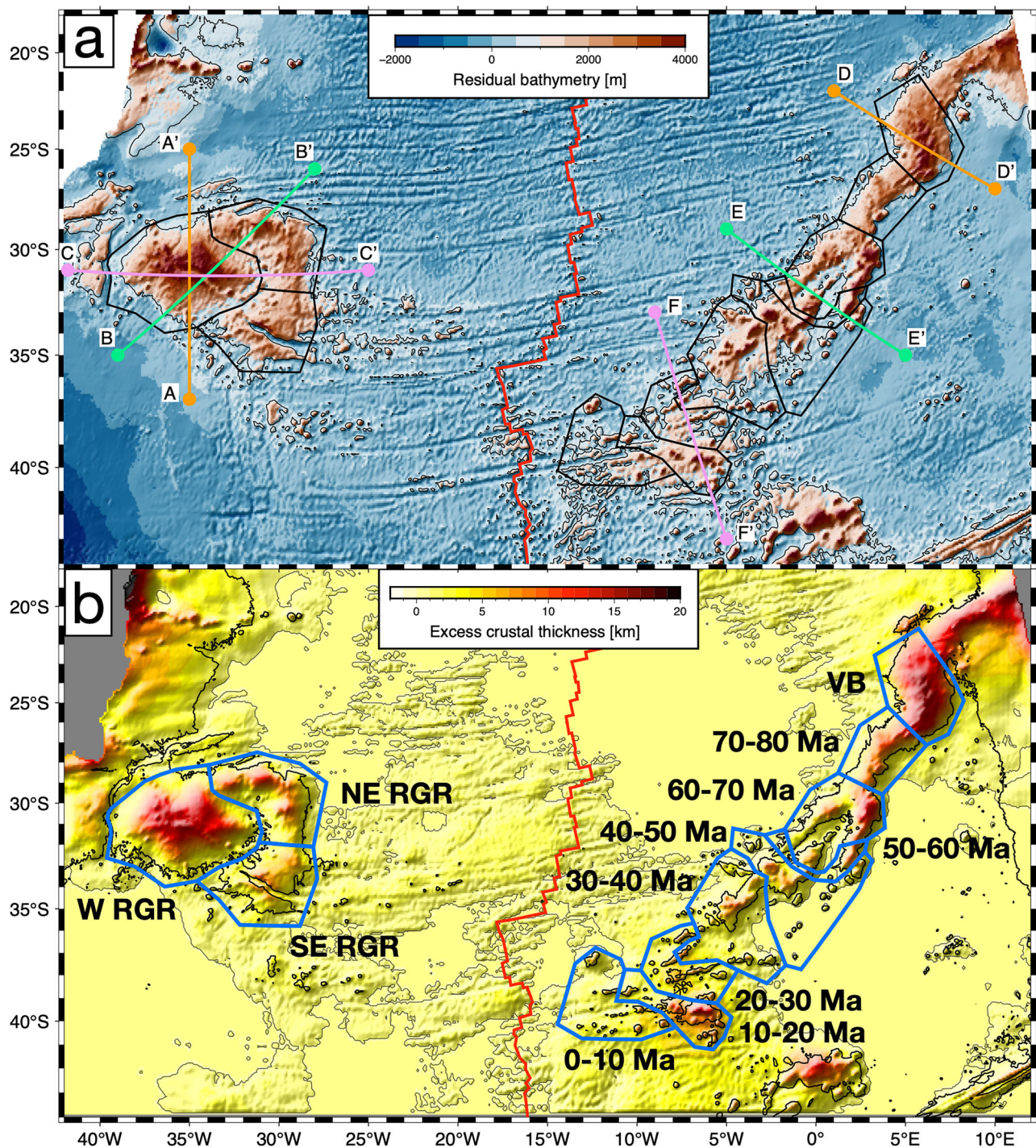
Fig. 7 | Excess volcanism from the T-G plume through time. a The residual bathymetry in the South Atlantic was used to calculate the extrusive volume of the T-G plume through time, using the 800 m contour (the thin black contour line), which is the closest contour to the break in slope throughout RGR/WR. Profiles A-A' through F-F' for RGR and WR can be found in Supplementary Fig 5. **b** Total magmatic volume generated by the T-G plume uses the excess crustal volume estimations from Huang & Li[52]. The subdivisions (outlined in black in (**a**) and blue in (**b**)) are based on the age of WR volcanism in 10 Myr increments, using ages from the literature[6,7,10,20,21], and for RGR include our W, NE, and SE subdivisions. The thin line denotes areas with excess volume, and the thick red line down the middle marks the MAR. Maps were made in GMT[70].

crushed with a steel jaw crusher and sieved to between ~100–175 and 250–300 μm and washed in water to remove fine-grained particles. Several phases were selected for dating and separated differently depending on the selected phase(s). Groundmass samples were magnetically separated using a Frantz magnetic barrier separator either once or twice, and the fraction with the least abundance of clearly altered grains was used. Samples were then leached first using 1 N and 6 N HCl, then 1 N and 3 N HNO$_3$ for one hour at each strength, and thoroughly rinsed with 18 mΩ distilled water after each leaching step. Plagioclase and other feldspars were separated also using a Frantz magnetic barrier separator, with progressively higher magnetic strengths until a relatively pure fraction of mostly feldspar remained. The feldspar concentrates were then leached the same way as groundmass, but with an additional 5% HF leach for between 3 and 5 min after the 3 N HNO$_3$ leach, and again thoroughly rinsed with 18 mΩ distilled water afterwards.

Table 2 | Magmatic production rates for RGR and WR

	Surface Area [km2]	Erupted Volume [km3]	Total Volume [km3]	Intrusive/Extrusive	Duration (max) [Myrs]	Duration (min) [Myrs]	Extrusive Eruption Rate (min) [km3/yr]	Extrusive Eruption Rate (max) [km3/yr]	Total Magma Production Rate (min) [km3/yr]	Total Magma Production Rate (max) [km3/yr]	Total Magma Production Rate per km Ridge Length (min) [km3/yr/km]	Total Magma Production Rate per km Ridge Length (max) [km3/yr/km]
W RGR	277,213	385,795	2,111,490	4.47	22	14	1.75E-02	2.76E-02	9.60E-02	1.51E-01	2.40E-04	3.77E-04
NE RGR	174,860	173,905	789,203	3.54	28	7	6.21E-03	2.48E-02	2.82E-02	1.13E-01	7.05E-05	2.82E-04
SE RGR	138,426	108,333	547,629	4.06	23	16	4.71E-03	6.77E-03	2.38E-02	3.42E-02	5.95E-05	8.56E-05
RGR Totals	590,498	668,034	3,448,321									
Valdivia Bank	148,837	242,747	1,816,748	6.48	22	14	1.10E-02	1.73E-02	8.26E-02	1.30E-01	2.06E-04	3.24E-04
WR 70-80 Ma	83,968	86,337	591,199	5.85	10	10	8.63E-03	8.63E-03	5.91E-02	5.91E-02	1.48E-04	1.48E-04
WR 60-70 Ma	136,664	162,201	643,695	2.97	10	10	1.62E-02	1.62E-02	6.44E-02	6.44E-02	1.61E-04	1.61E-04
WR 50-60 Ma	30,004	32,138	110,996	2.45	10	10	3.21E-03	3.21E-03	1.11E-02	1.11E-02	2.77E-05	2.77E-05
WR 40-50 Ma	88,613	84,098	235,729	1.80	10	10	8.41E-03	8.41E-03	2.36E-02	2.36E-02	5.89E-05	5.89E-05
WR 30-40 Ma	135,625	92,728	453,743	3.89	10	10	9.27E-03	9.27E-03	4.54E-02	4.54E-02	1.13E-04	1.13E-04
WR 20-30 Ma	62,918	27,085	379,509	13.01	10	10	2.71E-03	2.71E-03	3.80E-02	3.80E-02	9.49E-05	9.49E-05
WR 10-20 Ma	62,663	47,652	446,121	8.36	10	10	4.77E-03	4.77E-03	4.46E-02	4.46E-02	1.12E-04	1.12E-04
WR 0-10 Ma	69,830	27,752	298,597	9.76	10	10	2.78E-03	2.78E-03	2.99E-02	2.99E-02	7.46E-05	7.46E-05
Walvis Ridge Totals	819,122	802,738	4,976,338									
RGR + WR Totals	1,409,620	1,470,772	8,424,660									
RGR + WR Averages				5.55			5.59E-03	5.59E-03	3.63E-02	3.63E-02	9.07E-05	9.07E-05

Two glass samples were separated in part using a Frantz but mostly by handpicking fresh grains out from the matrix. One of these had a duplicate analyzed which was leached using our standard procedure described for groundmass above. Two biotite samples were separated using the 300-600 µm size fraction and the paper shake method where a small amount of grains are poured onto a sheet of paper and lightly shaken back and forth at an angle so that the rounder, non-biotite grains fall away, leaving almost only biotite remaining on the paper. The biotite samples were leached the same way as groundmass.

After leaching, samples were re-sieved to their original size fraction and hand-picked under a binocular microscope to remove any remaining altered grains, and feldspars with large or abundant melt inclusions. Samples were weighed and packed into Al-foil packets and labeled. Fish Canyon Tuff (FCT) sanidines were used as flux monitors (using the age of 28.201 ± 0.046 Ma[67]) and ten crystals (500–600 µm) were packed into Cu-foil packets. Samples and flux monitors were loaded into glass vials starting with a flux monitor and alternating between samples and flux monitors every two or three samples up to 7 cm in total length. The glass vials were vacuum-sealed with a blow torch and irradiated for six hours in Oregon State University's TRIGA reactor CLICIT facility. Two FCT flux monitor crystals were measured individually by total fusion and J-values were calculated by parabolic interpolation of the $^{39}Ar/^{40}Ar$ value of sequential FCT flux monitor measurements within a vial. Most samples had between 7 and 11 mg of material loaded into copper tray wells such that each was filled to 1 to 2 grains high. Samples were pre-cleaned at low laser power (between 0.2 and 0.8%) for 60 s prior to analysis. Samples were degassed for 60 s per step using a 30 W Synrad CO_2 laser with a Synrad FH Flyer marking head. Released gas was cleaned using three AP10 getters at 21 °C and one GP50 getter at 450 °C for 2 to 3 min before being expanded into the mass spectrometer. Between 20 and 50 incremental heating steps were measured using an ARGUS VI multi-collector mass spectrometer. ^{40}Ar, ^{39}Ar, ^{38}Ar, and ^{37}Ar were measured on faraday cups with 10^{13} Ω resistors (^{40}Ar was measured on a 10^{12} Ω resistor) and ^{36}Ar was measured using a CDD electron multiplier. Signals were regressed using exponential fits and abundances were extrapolated to time zero, defined as the moment the gas was introduced to the mass spectrometer from the extraction line. Blanks were measured at least every three steps after which a polynomial (up to fourth order) fit was applied and the signal subtracted from each step, while propagating blank uncertainties. Mass discrimination was calculated using a linear law relationship with the composition of air being 298.56 ± 0.31[68]. Collector calibrations were determined from air shot runs by "peak hopping" the ^{36}Ar signal between the L2 Faraday collector outfitted with a 10^{13} Ω resistor and the CDD electron multiplier, and those ratios were then used to correct the ^{36}Ar from the samples measured on the CDD electron multiplier. The decay constants from Min et al.[69] were used and the following production ratios were used: $^{36}Ar/^{37}Ar_{(Ca)} = 2.7 \times 10^{-4} \pm 0.17\%$; $^{38}Ar/^{37}Ar_{(Ca)} = 1.8 \times 10^{-4} \pm 9.63\%$; $^{39}Ar/^{37}Ar_{(Ca)} = 6.43 \times 10^{-4} \pm 0.92\%$; $^{40}Ar/^{39}Ar_{(K)} = 6.07 \times 10^{-4} \pm 9.65\%$; $^{38}Ar/^{39}Ar_{(K)} = 1.2077 \times 10^{-2} \pm 0.09\%$; all uncertainties are % 1σ standard deviations. Data reduction was done using ArArCALC[35] and Python.

Data availability
All $^{40}Ar/^{39}Ar$ data are available at the KArAr online data repository: https://doi.org/10.7288/V4/KArAr/15. All tables (including Supplementary Tables 1 & 2) are available in the supplementary excel file "Supplementary Data 1.xslx". The geologic samples used in this manuscript, and additional samples, can be found at the OSU Marine and Geology Repository.

References
1. Coffin, M. F. & Eldholm, O. Large igneous provinces: Crustal structure, dimensions, and external consequences. *Rev. Geophys.* **32**, 1–36 (1994).
2. Sager, W. W., Thoram, S., Engfer, D. W., Koppers, A. A. P. & Class, C. Late Cretaceous Ridge Reorganization, Microplate Formation, and the Evolution of the Rio Grande Rise – Walvis Ridge Hot Spot Twins, South Atlantic Ocean. *Geochem., Geophysics, Geosystems* **22**, e2020GC009390 (2021).
3. Hoyer, P. A. et al. Mantle plume and rift-related volcanism during the evolution of the Rio Grande Rise. *Commun. Earth Environ.* **3**, 1–10 (2022).
4. Bryan, S. E. & Ernst, R. E. Revised definition of Large Igneous Provinces (LIPs). *Earth-Sci. Rev.* **86**, 175–202 (2008).
5. Ussami, N., Chaves, C. A. M., Marques, L. S. & Ernesto, M. Origin of the Rio Grande Rise–Walvis Ridge reviewed integrating palaeogeographic reconstruction, isotope geochemistry and flexural modelling. *SP* **369**, 129–146 (2013).
6. O'Connor, J. M. & Duncan, R. A. Evolution of the Walvis Ridge-Rio Grande Rise Hot Spot System: Implications for African and South American Plate motions over plumes. *J. Geophys. Res.* **95**, 17475–17502 (1990).
7. Rohde, J. K., van den Bogaard, P., Hoernle, K., Hauff, F. & Werner, R. Evidence for an age progression along the Tristan-Gough volcanic track from new 40Ar/39Ar ages on phenocryst phases. *Tectonophysics* **604**, 60–71 (2013).
8. Schlömer, A., Geissler, W. H., Jokat, W. & Jegen, M. Hunting for the Tristan mantle plume – An upper mantle tomography around the volcanic island of Tristan da Cunha. *Earth Planet. Sci. Lett.* **462**, 122–131 (2017).
9. Homrighausen, S. et al. Evidence for compositionally distinct upper mantle plumelets since the early history of the Tristan-Gough hotspot. *Nat. Commun.* **14**, 3908 (2023).
10. O'Connor, J. M. & Jokat, W. Age distribution of Ocean Drill sites across the Central Walvis Ridge indicates plate boundary control of plume volcanism in the South Atlantic. *Earth Planet. Sci. Lett.* **424**, 179–190 (2015).
11. Barker, P. F., Carlson, R. L. & Johnson, D. A. *Initial Reports of the Deep Sea Drilling Project*, **72**. vol. 72 (U.S. Government Printing Office, 1983).
12. Guerra, J., Janasi, V., Srivastava, P., Basei, M. & Jovane, L. Major and trace-element mineral chemistry and implications for the petrogenesis of Eocene alkaline volcanic rocks from the western Rio Grande Rise, South Atlantic Ocean. in *Goldschmidt2021 abstracts* (European Association of Geochemistry, Virtual, 2021). https://doi.org/10.7185/gold2021.6348.
13. Mahoney, J. J., Storey, M., Duncan, R. A., Spencer, K. J. & Pringle, M. Geochemistry and age of the Ontong Java Plateau. in *Geophysical Monograph Series* (eds. Pringle, M. S., Sager, W. W., Sliter, W. V. & Stein, S.) **77** 233–261 (American Geophysical Union, Washington, D. C., 1993).
14. Duncan, R. A. A Time Frame for Construction of the Kerguelen Plateau and Broken Ridge. *J. Petrol.* **43**, 1109–1119 (2002).
15. Tejada, M. L. G. et al. New evidence for the Ontong Java Nui hypothesis. *Sci. Rep.* **13**, 8486 (2023).
16. Konrad, K. et al. Four distinct pulses of volcanism built the Melanesian Border Plateau: Implications for oceanic mid-plate superstructure formation. *Earth Planet. Sci. Lett.* **626**, 118549 (2024).
17. O'Connor, J. M. & Jokat, W. Tracking the Tristan-Gough mantle plume using discrete chains of intraplate volcanic centers buried in the Walvis Ridge. *Geology* **43**, 715–718 (2015).
18. Hoernle, K. et al. How and when plume zonation appeared during the 132 Myr evolution of the Tristan Hotspot. *Nat. Commun.* **6**, 7799 (2015).
19. Rohde, J. et al. 70 Ma chemical zonation of the Tristan-Gough hotspot track. *Geology* **41**, 335–338 (2013).
20. Schnur, S. Temporal Evolution of Submarine Volcanoes and Seamount Trails. (Oregon State University, Corvallis, OR, 2017).

Article

21. Homrighausen, S. et al. New age and geochemical data from the Walvis Ridge: The temporal and spatial diversity of South Atlantic intraplate volcanism and its possible origin. *Geochimica et. Cosmochimica Acta* **245**, 16–34 (2019).

22. Courtillot, V., Davaille, A., Besse, J. & Stock, J. Three distinct types of hotspots in the Earth's mantle. *Earth Planet. Sci. Lett.* **205**, 295–308 (2003).

23. Thiede, D. S. & Vasconcelos, P. M. Paraná flood basalts: Rapid extrusion hypothesis confirmed by new 40Ar/39Ar results. *Geology* **38**, 747–750 (2010).

24. Renne, P. R., Glen, J. M., Milner, S. C. & Duncan, A. R. Age of Etendeka flood volcanism and associated intrusions in southwestern Africa. *Geology* **24**, 659–662 (1996).

25. Ito, G. & Lin, J. Oceanic spreading center–hotspot interactions: Constraints from along-isochron bathymetric and gravity anomalies. *Geol* **23**, 657 (1995).

26. Gassmöller, R., Dannberg, J., Bredow, E., Steinberger, B. & Torsvik, T. H. Major influence of plume-ridge interaction, lithosphere thickness variations, and global mantle flow on hotspot volcanism—The example of Tristan. *Geochem., Geophysics, Geosystems* **17**, 1454–1479 (2016).

27. Whittaker, J. M. et al. Long-term interaction between mid-ocean ridges and mantle plumes. *Nat. Geosci.* **8**, 479–483 (2015).

28. Hanan, B. B., Kingsley, R. H. & Schilling, J.-G. Pb isotope evidence in the South Atlantic for migrating ridge—hotspot interactions. *Nature* **322**, 137–144 (1986).

29. Santos, R. V. et al. Dating Gondwanan continental crust at the Rio Grande Rise, South Atlantic. *Terra Nova* **31**, 424–429 (2019).

30. Mohriak, W. U., Nóbrega, M., Odegard, M. E., Gomes, B. S. & Dickson, W. G. Geological and geophysical interpretation of the Rio Grande Rise, south-eastern Brazilian margin: extensional tectonics and rifting of continental and oceanic crusts. *Pet. Geosci.* **16**, 231–245 (2010).

31. Davidson, P. C., Koppers, A. A. P., Class, C., Sager, W. W. & Heaton, D. 40Ar/39Ar dating reveals >30 Myrs of plume-ridge interaction formed the Rio Grande Rise (Dataset). Argon Geochronology Data Repository (KArAr FIESTA) https://doi.org/10.7288/V4/KArAr/15 (2025).

32. Koppers, A. A. P., Staudigel, H. & Duncan, R. A. High-resolution 40Ar/39Ar dating of the oldest oceanic basement basalts in the western Pacific basin. *Geochem., Geophys., Geosyst.* **4**, 8914 (2003).

33. Schaen, A. J. et al. Interpreting and reporting 40Ar/39Ar geochronologic data. *GSA Bull.* **133**, 461–487 (2020).

34. Wendt, I. & Carl, C. The statistical distribution of the mean squared weighted deviation. *Chem. Geol.: Isot. Geosci. Sect.* **86**, 275–285 (1991).

35. Koppers, A. A. P. ArArCALC—software for 40Ar/39Ar age calculations. *Computers Geosci.* **28**, 605–619 (2002).

36. Jiang, Q. et al. 40Ar/39Ar dating of basaltic rocks and the pitfalls of plagioclase alteration. *Geochimica et. Cosmochimica Acta* **314**, 334–357 (2021).

37. Davidson, P. C., Koppers, A. A. P., Sano, T. & Hanyu, T. A younger and protracted emplacement of the Ontong Java Plateau. *Science* **380**, 1185–1188 (2023).

38. Schoene, B. et al. U-Pb constraints on pulsed eruption of the Deccan Traps across the end-Cretaceous mass extinction. *Science* **363**, 862–866 (2019).

39. Burgess, S. D. & Bowring, S. A. High-precision geochronology confirms voluminous magmatism before, during, and after Earth's most severe extinction. *Sci. Adv.* **1**, e1500470 (2015).

40. Sprain, C. J. et al. The eruptive tempo of Deccan volcanism in relation to the Cretaceous-Paleogene boundary. *Science* **363**, 866–870 (2019).

41. Pérez-Díaz, L. & Eagles, G. Constraining South Atlantic growth with seafloor spreading data. *Tectonics* **33**, 1848–1873 (2014).

42. Thoram, S. et al. Nature and Origin of Magnetic Lineations Within Valdivia Bank: Ocean Plateau Formation by Complex Seafloor Spreading. *Geophys. Res. Lett.* **50**, e2023GL103415 (2023).

43. Seton, M. et al. A Global Data Set of Present-Day Oceanic Crustal Age and Seafloor Spreading Parameters. *Geochem., Geophys., Geosyst.* **21**, e2020GC009214 (2020).

44. Thoram, S. Tectonic Evolution of Oceanic Plateaus and Hotspot-Ridge Interactions: Walvis Ridge – Rio Grande Rise, South Atlantic and Tamu Massif, Pacific Ocean. (University of Houston, Houston, TX, 2021).

45. Graça, M. C., Kusznir, N. & Gomes Stanton, N. S. Crustal thickness mapping of the central South Atlantic and the geodynamic development of the Rio Grande Rise and Walvis Ridge. *Mar. Pet. Geol.* **101**, 230–242 (2019).

46. Gregg, T. K. P. & Fornari, D. J. Long submarine lava flows: Observations and results from numerical modeling. *J. Geophys. Res.: Solid Earth* **103**, 27517–27531 (1998).

47. Michael, P. J., Zhang, J. & Trowbridge, S. R. Earth's longest lava flows erupted from its largest igneous province: The submarine Ontong Java Plateau. *Earth Planet. Sci. Lett.* **644**, 118905 (2024).

48. Doubrovine, P. V., Steinberger, B. & Torsvik, T. H. Absolute plate motions in a reference frame defined by moving hot spots in the Pacific, Atlantic, and Indian oceans. *J. Geophys. Res.: Solid Earth* **117**, B09101 (2012).

49. Müller, R. D. et al. A tectonic-rules-based mantle reference frame since 1 billion years ago – implications for supercontinent cycles and plate–mantle system evolution. *Solid Earth* **13**, 1127–1159 (2022).

50. Torsvik, T. H., Müller, R. D., Van der Voo, R., Steinberger, B. & Gaina, C. Global plate motion frames: Toward a unified model. *Rev. Geophys.* **46**, RG3004 (2008).

51. Bai, Y. et al. Mantle plume – mid ocean ridge interactions revealed from hotspot melt production rate along the Walvis Ridge-Rio Grande Rise. *Earth Planet. Sci. Lett.* **648**, 119102 (2024).

52. Huang, L. & Li, C.-F. What controls the magma production rate along the Walvis Ridge, South Atlantic?. *Tectonophysics* **883**, 230381 (2024).

53. Adam, C., Vidal, V. & Escartín, J. 80-Myr history of buoyancy and volcanic fluxes along the trails of the Walvis and St. Helena hotspots (South Atlantic). *Earth Planet. Sci. Lett.* **261**, 432–442 (2007).

54. Crosby, A. G. & McKenzie, D. An analysis of young ocean depth, gravity and global residual topography. *Geophys. J. Int.* **178**, 1198–1219 (2009).

55. Sykes, T. J. S. A correction for sediment load upon the ocean floor: Uniform versus varying sediment density estimations—implications for isostatic correction. *Mar. Geol.* **133**, 35–49 (1996).

56. Weatherall, P. et al. A new digital bathymetric model of the world's oceans. *Earth Space Sci.* **2**, 331–345 (2015).

57. Richards, M. A. et al. Triggering of the largest Deccan eruptions by the Chicxulub impact: Reply. *Geol. Soc. Am. Bull.* **129**, 256–256 (2017).

58. Gladczenko, T. P. et al. South Atlantic volcanic margins. *JGS* **154**, 465–470 (1997).

59. Gladczenko, T. P., Coffin, M. F. & Eldholm, O. Crustal structure of the Ontong Java Plateau: Modeling of new gravity and existing seismic data. *J. Geophys. Res.: Solid Earth* **102**, 22711–22729 (1997).

60. White, S. M., Crisp, J. A. & Spera, F. J. Long-term volumetric eruption rates and magma budgets. *Geochem., Geophys., Geosyst.* **7**, Q03010 (2006).

61. Smallwood, J. R. & White, R. S. Ridge-plume interaction in the North Atlantic and its influence on continental breakup and seafloor spreading. *Geol. Soc., Lond., Spec. Publ.* **197**, 15–37 (2002).

62. Sallarès, V. & Charvis, P. Crustal thickness constraints on the geodynamic evolution of the Galapagos Volcanic Province. *Earth Planet. Sci. Lett.* **214**, 545–559 (2003).

63. Ito, G., Lin, J. & Gable, C. W. Dynamics of mantle flow and melting at a ridge-centered hotspot: Iceland and the Mid-Atlantic Ridge. *Earth Planet. Sci. Lett.* **144**, 53–74 (1996).

64. Beier, C. et al. The submarine Azores Plateau: Evidence for a waning mantle plume?. *Mar. Geol.* **451**, 106858 (2022).

65. Sager, W. W., Sano, T. & Geldmacher, J. Formation and evolution of Shatsky Rise oceanic plateau: Insights from IODP Expedition 324 and recent geophysical cruises. *Earth-Sci. Rev.* **159**, 306–336 (2016).

66. Kasbohm, J., Schoene, B. & Burgess, S. Radiometric Constraints on the Timing, Tempo, and Effects of Large Igneous Province Emplacement. in *Large Igneous Provinces* 27–82 (American Geophysical Union (AGU), 2021). https://doi.org/10.1002/9781119507444.ch2

67. Kuiper, K. F. et al. Synchronizing Rock Clocks of Earth History. *Science* **320**, 500–504 (2008).

68. Lee, J.-Y. et al. A redetermination of the isotopic abundances of atmospheric Ar. *Geochimica et. Cosmochimica Acta* **70**, 4507–4512 (2006).

69. Min, K., Mundil, R., Renne, P. R. & Ludwig, K. R. A test for systematic errors in 40Ar/39Ar geochronology through comparison with U/Pb analysis of a 1.1-Ga rhyolite. *Geochimica et. Cosmochimica Acta* **64**, 73–98 (2000).

70. Wessel, P. et al. The Generic Mapping Tools Version 6. *Geochem., Geophysics, Geosystems* **20**, 5556–5564 (2019).

71. GEBCO Bathymetric Compilation Group 2023. The GEBCO_2023 Grid - a continuous terrain model of the global oceans and land. NERC EDS British Oceanographic Data Centre NOC https://doi.org/10.5285/F98B053B-0CBC-6C23-E053-6C86ABC0AF7B (2023).

72. Müller, R. D. et al. GPlates: Building a Virtual Earth Through Deep Time. *Geochem., Geophysics, Geosystems* **19**, 2243–2261 (2018).

73. Zahirovic, S. et al. Subduction and carbonate platform interactions. *Geosci. Data J.* **9**, 371–383 (2022).

Acknowledgements

Author contributions

Competing interests

The authors declare no competing interests.

Additional information

Supplementary information The online version contains supplementary material available at https://doi.org/10.1038/s43247-025-02572-y.

Correspondence and requests for materials should be addressed to Peter C. Davidson.

Peer review information *Communications Earth & Environment* thanks Valerie Finlayson, Maria Tejada, Brian Jicha and the other, anonymous, reviewer(s) for their contribution to the peer review of this work. Primary Handling Editors: Domenico Doronzo, Joe Aslin and Carolina O.

Reprints and permissions information is available at http://www.nature.com/reprints

Publisher's note Springer Nature remains neutral with regard to jurisdictional claims in published maps and institutional affiliations.